Accurate Transonic Wave Drag Prediction Using Simple Physical Models

Josef Mertens,* Karl D. Klevenhusen,† and Heinz Jakob‡
Messerschmidt-Bölkow-Blohm GmbH, Bremen, Federal Republic of Germany

A new method is presented to compute the transonic wave drag of airfoils. Coupled with an inverse boundary-layer procedure, the calculated results have an accuracy comparable to experiments. The method is robust and easy to handle without the necessity of tuning; hence, it is an excellent engineering tool for supercritical airfoil design. The inviscid flowfield is assumed to be governed by the full potential equation except at the shock. The solution is obtained by a finite-difference method. At shock points, a shock operator is introduced; it satisfies the kinematic Prandtl relation for normal and oblique shocks, which is the consistent condition for the velocity potential. For each streamline behind the shock, an entropy correction is calculated by the Rankine-Hugoniot equations. The wave drag is given by integrating the entropy rise along the shock. The computational mesh, formed by incompressible stream and potential lines, allows easy coupling of the boundary-layer solution at the airfoil and wake. The H-type singularity at the incompressible stagnation point is handled by a finite-volume procedure. For better physical pressure and drag solutions, the condition of the normal shock has to be altered due to the boundary layer. Therefore, an analytic model of the inviscid interference region was developed and the essential features are embedded in the numerical procedure.

Nomenclature

A = defined by Eq. (2)
a = speed of sound
$\bar{a}^*$ = reduced critical speed for oblique shock defined by Eq. (8)
AL = angle of attack
B = Prandtl correction of shock operator, Eq. (4)
C_D, CD = drag coefficient
C_L, CL = lift coefficient
C_p, CP = pressure coefficient
C_v = specific heat, constant volume
D^- = backward difference
D = central difference
D_w = wave drag
dF = area element of shock, Eq. (14)
K = Bernoulli constant, Eqs. (11), (12)
L = profile chord
l = length of shock interference region
M = Mach number
P = static pressure
$PrOp$ = Prandtl operator, Eqs. (3), (4), (6-8)
s = specific entropy
u = velocity value
x, z = Cartesian coordinates
Z = assumed focus of compression wave, Fig. 7
α = Mach angle
γ = quotient of specific heats
Δx = grid spacing, x direction
δ_1 = displacement thickness of boundary layer
$\hat{\delta}_1$ = rise of displacement thickness in interference region
Θ = shock angle
ϑ = deflection angle of streamline
ρ = density
ϕ = velocity potential
Ω = region

Subscripts

L = lower side of trailing edge, Eqs. (15-17)
m = shock with maximum deflection angle
U = upper side of trailing edge, Eqs. (15-17)
Z = focus point, Figs. 7 and 8
δ = flow conditions at the boundary-layer border upstream of the shock interference region, Fig. 7, region Ω_1
0 = stagnation conditions
∞ = freestream conditions

Superscripts

$(\ )^*$ = critical conditions at $u = a =: a^*$
$(\hat{\ })$ = immediately behind shock

Introduction

DRAG prediction at transonic speeds is still a difficult task even for planar flow. There are two typical deficiencies when calculating drag by integration of pressure in modern numerical methods.

First, the integration may be inaccurate due to numerical errors caused by a crude grid size, a solution that has not fully converged, or simply integration errors. Clearly, one can improve the results by refining or optimizing the grid size or the integration procedure, but this would cause an increased numerical effort that is not desirable and, as will be shown, not necessary.

Furthermore, it is well known that in subsonic cases boundary-layer methods are useful for predicting not only skin-friction drag, but also momentum drag, which is the sum of pressure drag and skin-friction drag. Hence, there is no need to integrate the pressure at subsonic speeds. However, at transonic speeds, shocks may occur and the total drag is the sum of boundary-layer momentum drag and wave drag. In this case, a correct drag prediction by common numerical methods is not possible if they cannot

---

Received Nov. 12, 1985; presented as Paper 86-0512 at the AIAA 24th Aerospace Sciences Meeting, Reno, NV; Jan. 6-9, 1986; revision received Oct. 14, 1986. Copyright © American Institute of Aeronautics and Astronautics, Inc., 1987. All rights reserved.

*Research Scientist, Civil Transport Aircraft Division. Member AIAA.

†Head of Theoretical Aerodynamics, Civil Transport Aircraft Division.

‡Research Scientist, Civil Transport Aircraft Division.

describe the physical phenomenon of the shock itself and of the shock/boundary-layer interaction in sufficient detail.

The present paper shows a simple way of fitting the physical phenomena of entropy increase and shock/boundary-layer interaction into a method based on the full potential equation, which in its original form cannot describe these phenomena. But these improvements enable the method to predict wave drag in a manner that is physically correct.

Basic Inviscid Method

Full Potential Equation

The governing equation for the present analysis is the quasilinear full potential equation

$$(\alpha^2-\phi_x^2)\phi_{xx}+(\alpha^2-\phi_z^2)\phi_{zz}-2\phi_x\phi_z\phi_{xz}=0 \tag{1}$$

This equation is strictly valid for the flowfield in front of a shock; it describes quite well the flow behind a weak shock, although it is not valid at the shock itself.

The numerical treatment of this equation is well proved by Bauer-Garabedian's method[1] using the finite-difference scheme of Murman-Cole[2] and including a conservative shock point operator.[3] From a mathematical point of view, conservative schemes are more correct than nonconservative ones. However, compared with experimental data or the results of Euler codes,[4] nonconservative codes give much better results. The reason for this effect is that the isentropic mass production simulates the entropy increase at a shock in real flow.

Shock Point Operator

Adding to the results of several other authors dealing with entropy corrections,[5-14] a shock point operator for Eq. (1) was found[15] to satisfy Prandtl's equation.

Assuming one-dimensional flow, Eq. (1) reduces to

$$A:=(a^2-\phi_x^2)\phi_{xx}=0 \tag{2}$$

Then, at shock point i (see Fig. 1), a finite-difference operator is introduced by

$$D^-A+DA+B=0 \tag{3}$$

with

$$B:=\frac{1}{\Delta x}\cdot\frac{\gamma+1}{6}(u_{i+1/2}-u_{i-3/2})^3 \tag{4}$$

D^- denotes the backward and D the central differencing of A. D^-A+D^+A is the well-known Murman operator.[3] This means that the so-called Prandtl operator (*PrOp*) is actually Murman's operator with the addition of a usually nonzero term. Hence, the new operator is not "conservative."

The shock point i is detected when central differencing indicates subsonic flow and backward differencing supersonic flow.

One can show that this *PrOp* satisfies exactly

$$u_{i-3/2}\cdot u_{i+1/2}=a^{*2} \tag{5}$$

which is known as Prandtl's equation.

This is the consistent condition of a shock point operator within the framework of the full potential equation, because Prandtl's equation is pure kinematic, as is the velocity potential.

In the case of oblique shocks, which is very important for shock/boundary-layer interaction, instead of Eq. (4), one gets

$$B:=\frac{1}{\Delta x}\cdot\frac{\gamma+1}{6}[(u_{i+1/2}-u_{i-3/2})^3$$

$$+3(\bar{a}^{*2}-a^{*2})(u_{i+1/2}-u_{i-3/2})] \tag{6}$$

This operator satisfies the equation

$$u_{i-3/2}\cdot u_{i+½}=\bar{a}^{*2} \tag{7}$$

with

$$\bar{a}^{*2}:=\frac{a^{*2}-(\gamma-1)/(\gamma+1)\cdot u_{i-3/2}^2\cdot\cos^2\Theta}{\sin\Theta\cdot\sin(\Theta-\vartheta)} \tag{8}$$

which is Prandtl's equation for oblique shocks with shock angle Θ and deflection angle ϑ. In Eqs. (7) and (8), it should be noted that the velocities are not normal to the shock, but in the streamline direction.

These shock point operators were fitted into a finite-difference code in the same manner as Murman's operator by Garabedian-Korn.[1] When using the *PrOp*, the computed flowfield is still irrotational behind a shock, but the calculated velocity jump across the shock is physically correct.

Applying the conservation laws of mass

$$\rho u=\hat{\rho}\hat{u} \tag{9}$$

and momentum

$$\rho u^2+p=\hat{\rho}\hat{u}^2+\hat{p} \tag{10}$$

(or energy) at the shock, $\hat{\rho}$ and $\hat{p}$ can be calculated, where ($\hat{}$) indicates values behind the shock. Then, it follows that

$$\hat{K}:=\hat{p}/\hat{\rho}^\gamma \tag{11}$$

which is constant along a streamline behind the shock. Hence, the constants in front of the shock

$$K:=p/\rho^\gamma \tag{12}$$

and behind the shock [Eq. (11)] are quite different, but physically correct. From this difference, an entropy jump, which must be taken into account when determining pressure coefficients C_p, can be calculated.

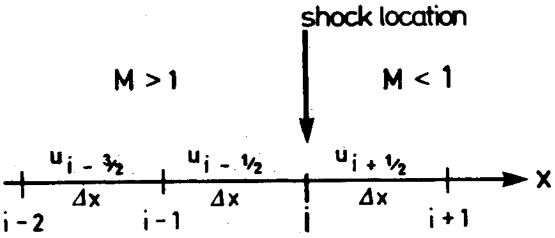

Fig. 1 Streamline points at the shock.

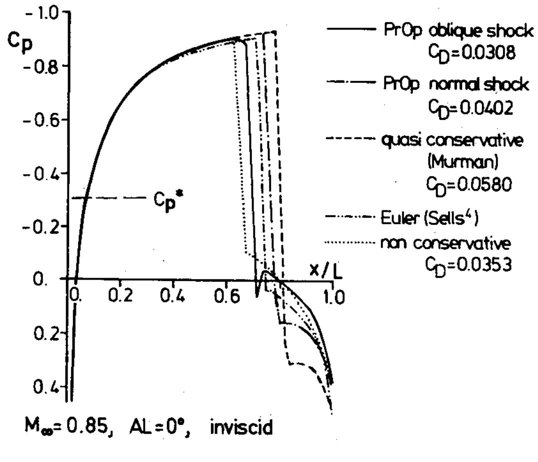

Fig. 2 NACA 0012, comparison of shock point operators.

Wave Drag

The entropy jump across the shock is given by

$$\hat{s}-s=C_v \ln(\hat{K}/K) \tag{13}$$

Then, the wave drag is determined by Oswatitsch's[16] formula integrating along shock lines,

$$D_W=\frac{1}{u_\infty}\int_{\text{Shock}}\frac{a^{*2}}{\gamma(\gamma-1)}\rho u\frac{\hat{s}-s}{C_v}\mathrm{d}F \tag{14}$$

The numerical evaluation of this integral was found to be much more accurate than integration of the pressure around the airfoil.

Thus, the *PrOp* combined with the past shock corrections [Eqs. (9) and (10)] satisfies all the Rankine-Hugoniot conditions in the streamline direction. The tangential Rankine-Hugoniot condition is identically fulfilled since the potential must not have a jump.

Kutta Condition

When shocks occur, there are usually different constants K at the upper and lower sides of the trailing edge of an airfoil. This, of course, affects the Kutta condition.

A common Kutta condition consists of equal static pressure at both sides of the trailing edge,

$$P_U-P_L=0 \tag{15}$$

This leads to the condition

$$u_U-u_L=0 \tag{16}$$

in isentropic flow and to

$$u_U-u_L=\left(\frac{2a_0^2}{\gamma-1}-u_L^2\right)\frac{1-(K_U/K_L)^{1/\gamma}}{u_U+u_L} \tag{17}$$

in the case of different constants K_L and K_U. When using Kutta condition [Eq. (17)], there is a jump of tangential velocities at the trailing edge that must be carried on along a wake line behind the airfoil up to infinity. Numerical investigations showed that it is not necessary to apply Eq. (17) if the local Mach numbers are <1.3 in front of the shock.

The effects of several shock operators are displayed in Fig. 2. When applying Murman's operator, we obtain unrealistic shock locations and strengths. On the other hand, the present normal *PrOp* shifts the shock position upstream and reduces its strength. This is a typical feature of nonconservative schemes and the effect increases when applying oblique *PrOp* with the assumption of shock inclination. Nevertheless, in this case, the shock is standing some distance downstream from the shock determined by a common nonconservative scheme.

The present method of allowing entropy changes is a potential approximation to the Euler equations. It yields results that agree very well with those of Euler codes.[15]

Grid

An optimal computational grid for numerical methods should be carefully adapted to the mathematical, numerical, geometrical, and physical aspects of the problem. We chose a grid of H-type, formed by the potential and streamlines of incompressible flow around the given airfoil.[17] (See Fig. 3.) This closely aligns the grid with the compressible streamlines, so that it is unnecessary to use a rotated difference scheme. Furthermore, the grid line arising from the trailing edge gives a reasonable estimate for a wake, which has to be used as a communication line between the potential and boundary-layer calculations.

One disadvantage of the H-grid topology is that the transformation from the physical to computational plane is singular at the stagnation points of incompressible flow at the leading and trailing edges of the profile. Consequently, these points must be handled separately.[18,19]

First, the front stagnation point S will always be chosen as a node point of the grid. In order to get an updated value for the velocity potential in the relaxation process at S, a finite volume is cut out of the flowfield (Fig. 4). Velocity and density are calculated at the corner points 1-9 by numerical differentiation of the potential. The equation of mass conservation is then solved for the unknown potential value at the singular point S.

A tangential velocity component is allowed at the singular point S, i.e., the compressible stagnation point need not

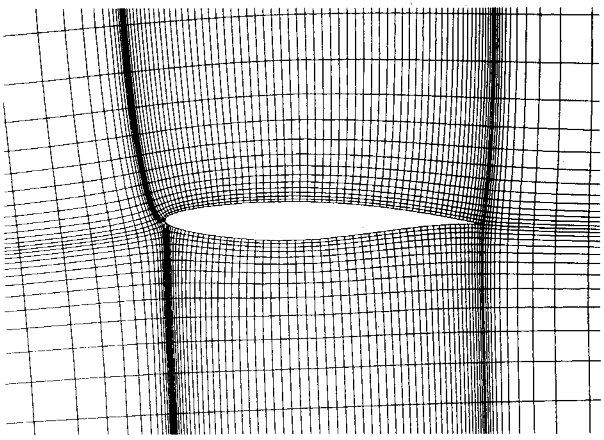

Fig. 3 Streamline coordinates.

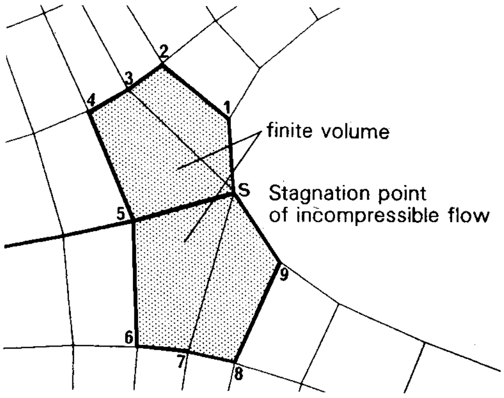

Fig. 4 Finite volume at incompressible stagnation point.

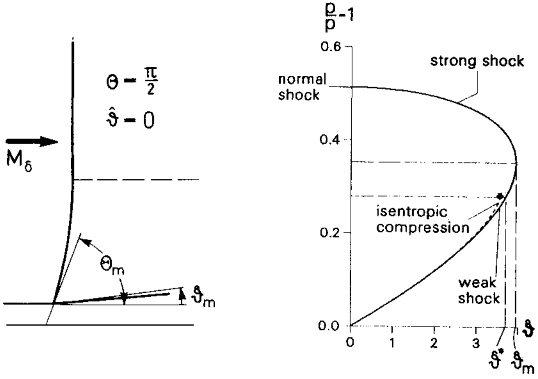

Fig. 5 One-shock model, $M_\delta=1.2$.

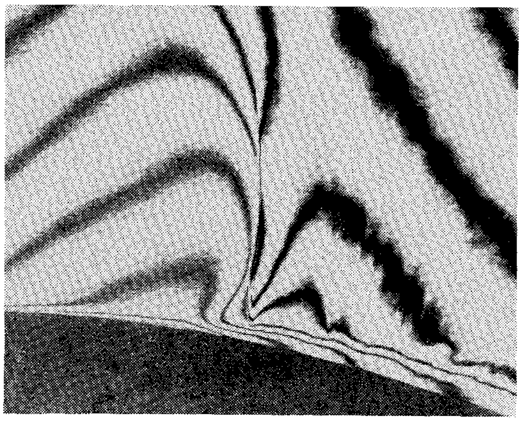

Fig. 6 Interferogram, $M_\delta = 1.36$.

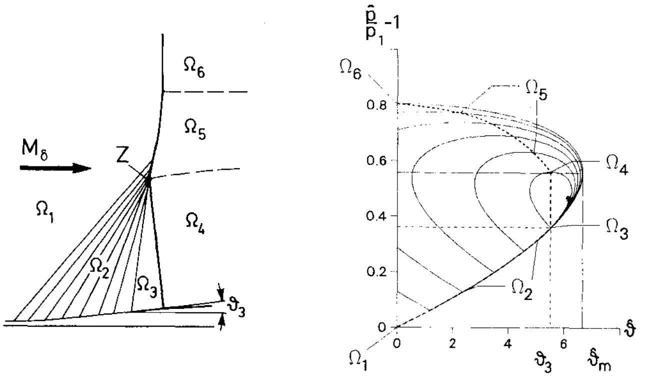

Fig. 7 Real configuration, $M_\delta = 1.3$.

coincide with S. This is easily verified by choosing different angles of attack for the H-grid and the onset flow. The compressible stagnation point then varies substantially from S, but the calculated transonic flow shows only minor changes within the overall accuracy.

We never make the trailing edge of the profile a node point of the grid. Instead, there are two node points slightly inside the profile at the upper and lower surfaces that are used to control the Kutta condition. The velocities at these points are determined by differencing across the trailing edge from the contour onto the wake line.

Shock/Boundary-Layer Interference Model

Shock Conditions at the Boundary Layer

At the wing surface, the normal shock interacts with the boundary layer. Until now, this strong interference problem has not been adequately resolved and most solutions produce wrong pressure and drag results.

In the slow boundary layer, flow pressure disturbances can proceed upstream, thus diminishing the pressure jump across the shock. Weakening of the shock is coupled with an inclination Θ of the shock,[20] as can be seen in the shock polar $\hat{p}(\vartheta)$ in Fig. 5. For stable subsonic downstream conditions, the weakest shock strength is reached at the maximum deflection angle $\hat{\vartheta}_m$ with shock inclination Θ_m. A transition is required from the normal shock in the outer flow region to the oblique shock at the boundary layer. Figure 5 shows the weakening of the strong shock belonging to the upper part of the shock polar $\hat{p}(\hat{\vartheta})$.

A reduction of pressure jump not only occurs by shock weakening, but also—and more effectively—by spreading of the pressure rise. The upstream propagating disturbances in the boundary layer split the oblique shock into an isentropic compression wave followed by a strong shock, a so-called "Mach shock." This phenomenon occurs in high-resolution experiments,[21,22] as shown in Fig. 6. Reaching higher preshock Mach numbers $M_\delta \gtrsim 1.3$, the boundary-layer separates and the upstream compression wave begins to converge into a weak shock.

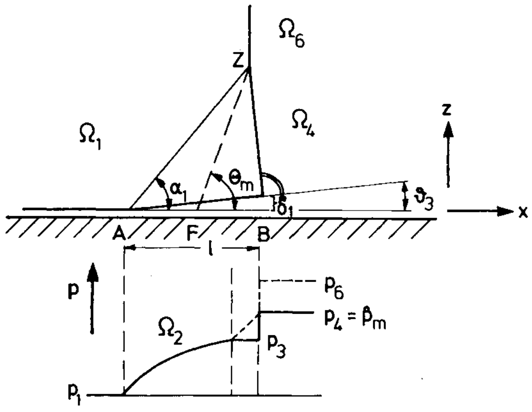

Fig. 8 Approximate method.

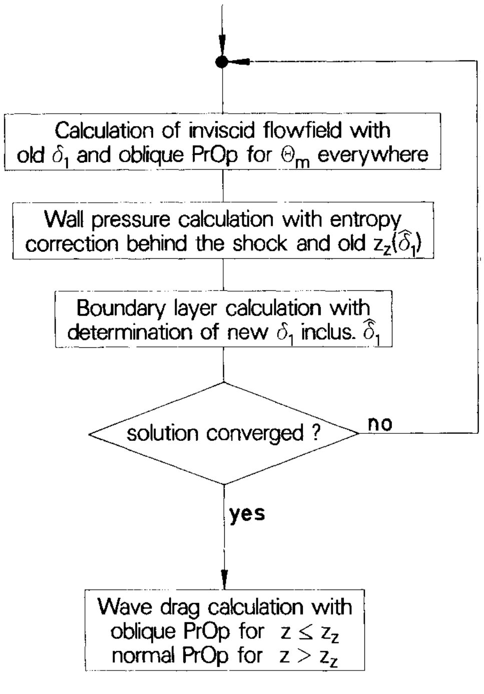

Fig. 9 Calculation cycle of viscid-inviscid interaction.

Approximate Solution of the Shock/Boundary-Layer Interaction

Figure 7 shows the situation of the flow in Fig. 6 at $M_\delta \lesssim 1.3$ where the incoming supersonic flow is assumed homogeneous (Ω_1). In the outer flow, there is a normal shock between Ω_1 and Ω_6. Between Ω_1 and Ω_5, the shock weakens and inclines. Ω_2 is the induced compression wave nearly focusing at Z. Behind Ω_2 is a small homogeneous region Ω_3, terminated by the Mach shock and the homogeneous subsonic downstream region Ω_4.

For the approximate solution of the inviscid part of the interference region, the compression wave Ω_2 is assumed to be focused at Z. (For a combination of a focused compression wave, an oblique outer shock with inclination Θ_m, and a Mach shock, solutions at the triple point Z exist for

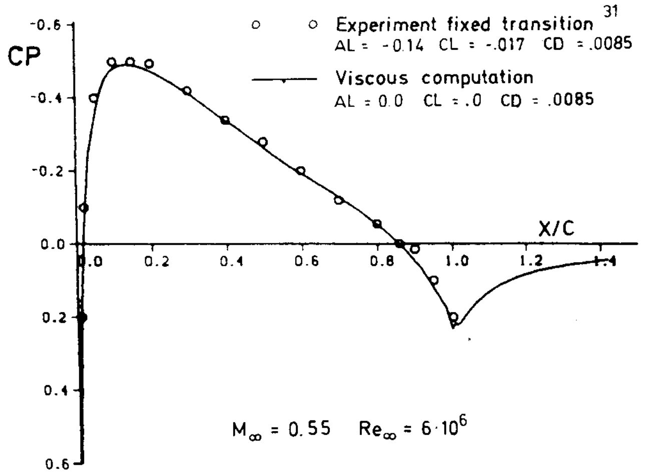

Fig. 10 NACA-0012, subsonic flow.

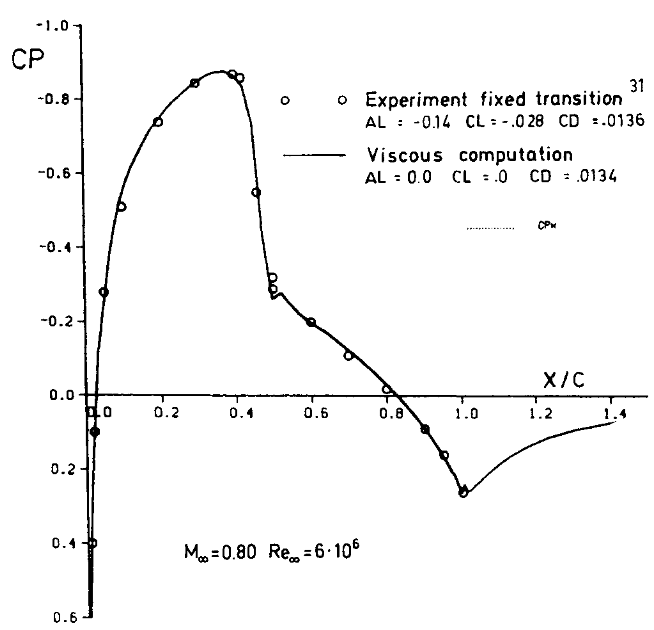

Fig. 11 NACA-0012, transonic flow.

preshock Mach numbers $M_\delta > \sqrt{2}$.) In good agreement with experiment,[21,22] we use as postshock condition at Z and in Ω_4 the postshock pressure $\hat{p}_m$ of the maximum deflection angle $\hat{\vartheta}_m$; thus, the deflection angle $\hat{\vartheta}_m$ itself cannot be reached ($M_\delta < \sqrt{2}$). In addition, the Mach shock between Ω_3 and Ω_4 is assumed to be normal.

These assumptions result in a closed solution[23] for the focused compression wave Ω_2, the homogeneous region Ω_3 terminated by the Mach shock, and the homogeneous subsonic downstream region Ω_4. For air ($\gamma = 1.4$), it yields $\hat{p}_m$ given by the shock polar,

$$\hat{p}_m = p_1 \cdot 1/2 \cdot \{M_\delta^2 - 2 + [M_\delta^4 + 4/3 \cdot (5 + M_\delta^2)]^{1/2}\} \tag{18}$$

Combining the isentropic pressure rise

$$p_3 = p_1 \cdot \left(\frac{5 + M_\delta^2}{5 + M_3^2}\right)^{7/2} \tag{19}$$

and $\hat{p}_m / p_3$ at the normal Mach shock results in

$$\frac{\hat{p}_m}{p_1} = \frac{7M_3^2 - 1}{6}\left(\frac{5 + M_\delta^2}{5 + M_3^2}\right)^{7/2} \tag{20}$$

where $M_3^2 - 1 \ll 1$ holds. The second respective first-order solution is

$$M_3^2 - 1 \doteq \frac{12}{19}\left(1 - \left\{1 - \frac{38}{7}\left[\frac{\hat{p}_m}{p_1}\left(\frac{6}{5 + M_\delta^2}\right)^{7/2} - 1\right]\right\}^{1/2}\right)$$

$$\doteq \frac{12}{7}\left[\frac{\hat{p}_m}{p_1}\left(\frac{6}{5 + M_\delta^2}\right)^{7/2} - 1\right] \tag{21}$$

The streamline angle ϑ_3 is given by a characteristics solution of the isentropic field Ω_2

$$\vartheta_3 = \arcsin\left(\frac{\sqrt{M_3^2 - 1} - \sqrt{M_\delta^2 - 1}}{M_\delta \cdot M_3}\right)$$

$$+ \sqrt{6} \cdot \arctan\left(\sqrt{6}\,\frac{\sqrt{M_\delta^2 - 1} - \sqrt{M_3^2 - 1}}{6 + \sqrt{M_\delta^2 - 1}\sqrt{M_3^2 - 1}}\right) \tag{22}$$

As for the region Ω_3, Eqs. (19) and (22) hold for the compression wave Ω_2 with index 2 instead of 3 and $M_\delta > M_2 > M_3$; the Mach number distribution M_2 is given with focus Z at (x_z, z_z) as

$$M_2(x) = 6\tan^2\left[\arctan\sqrt{\frac{M_\delta^2 - 1}{6}}\right.$$

$$\left. + \frac{1}{\sqrt{6}}\left(\arcsin\frac{1}{M_\delta} - \arctan\frac{z_z}{x_z - x}\right)\right] + 1 \tag{23}$$

This solution includes the shape of the boundary-layer ramp (given by a streamline at the border) and the pressure distribution. Due to the geometric similarity, there remains one parameter z_z for the determination of the size of the region. It can be calculated by the increase of the displacement thickness $\hat{\delta}_1$

$$z_z = \frac{\hat{\delta}_1}{M_\delta \cdot \sin\vartheta_3 \cdot \cos(\alpha_1 - \vartheta_3)}, \quad \sin\alpha_1 := \frac{1}{M_\delta} \tag{24}$$

or the length of the interference region l,[24]

$$z_z = l\,\frac{1 + \tan^2\vartheta_3}{\cot\alpha_1 + \tan\vartheta_3} \tag{25}$$

A summary of the approximate method is shown in Fig. 8 and

$$\sin^2\Theta_m = \frac{6(\hat{p}_m/p_1) + 1}{7M_\delta^2} \tag{26}$$

Numerical Method

When applying numerical methods, it is sufficient for the pressure calculation to assume a normal shock in the outer region between Ω_1 and Ω_6 ($z > z_z$, see top of Fig. 8) and an oblique shock with a pressure jump to $\hat{p}_m$ in the inviscid interference region between Ω_1 and Ω_4 ($z \le z_z$). The size of the interference region is obtained prescribing $\hat{\delta}_1$ or l according to Fig. 8. In contrast to the computed pressure jump at point F, a resolution of the pressure distribution along AB is analytically prescribed for the boundary-layer computation. The displacement thickness δ_1 is growing with grad p in the boundary-layer equations; however, because the inverse for the analytical solution along AB holds, grad $p \sim 1/\delta_1$, a solution can be achieved by continuing the iterations of the viscid-inviscid interaction.[25] The entropy in Ω_4 ($z \le z_z$) is given by the entropy rise at the Mach shock.

This interference model was embedded in a full potential code using the above-introduced shock operator. In Fig. 9, the pressure distribution is computed with a shock inclina-

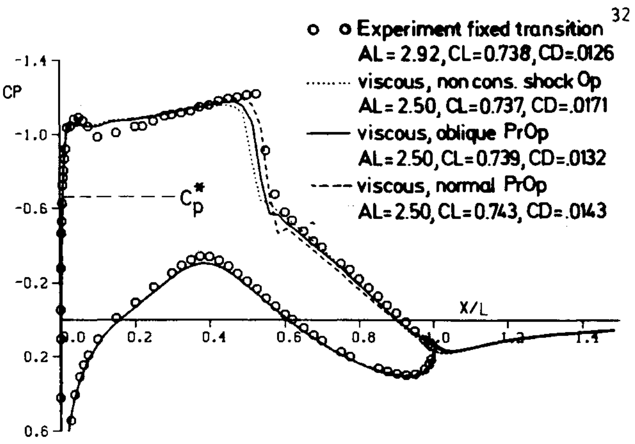

Fig. 12 RAE-2822, $M_\infty=0.73$, $Re_\infty=6.5\times10^6$.

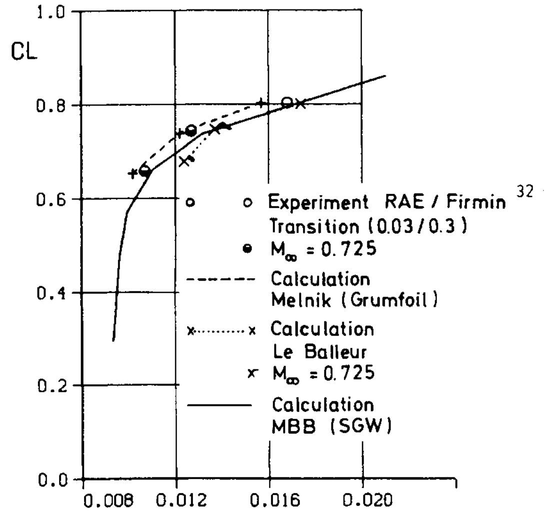

Fig. 13 RAE-2822, $M_\infty=0.73$, $Re_\infty=6.5\times10^6$.

tion Θ_m everywhere; it is the right condition at the airfoil boundary and gives minor errors in the outer field due to the small shock strength there. On the other hand, the wave drag is determined with an oblique shock for $z\leq z_z$ and a normal shock in the outer field $z>z_z$. This splitting of the shock computation between the pressure distribution and wave drag is necessary because a potential method cannot resolve the slip line belonging to the change in shock strength at Z.

Boundary-Layer Method

The calculation scheme outlined in the previous section was incorporated in a viscous-inviscid interaction method[25] that allowed treatment of the strong interaction regions by a semi-inverse matching procedure coupling the outer inviscid flow with an inverse boundary-layer integral method.[26] The turbulent closure for separated flows is based on Alber's similar solution.[27] The empirical relations of the Walz method[28] are used for turbulent attached boundary layers. The laminar boundary layer is calculated by a modified Walz method,[29] which computes transition by an empirical relation of Thiede.[30]

Limitations of the Model

The presented model describes shock/boundary-layer interaction by changing the inviscid boundary condition of a normal shock to a maximum weakening of the shock by the boundary layer. This is valid as long as the boundary layer does not separate at the shock; for turbulent boundary layers, this is $M_\delta\lesssim1.3$. When the boundary layer separates, the shock weakening decreases and the compression wave converges to a weak shock resulting in a λ shock. Now the pressure p_4 behind the shock cannot be prescribed and there is a strong coupling of the numerical solutions.[23] However, this problem is beyond the scope of the present paper.

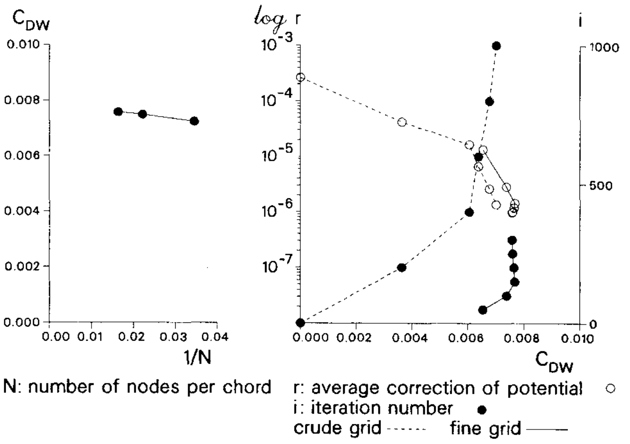

Fig. 14 Wave drag accuracy, NACA 0012, $M_\infty=0.8$, $AL=0$.

Results

Examples

Wave drag is a physical phenomenon of inviscid flow. Hence, we cannot compare computed wave drag with experimental data. Boundary-layer effects must be taken into account.

Figure 10 demonstrates the quality of the method for a subsonic case. The wave drag is exactly zero and the computed drag is identical to the momentum drag computed by the boundary-layer method. In this case, there is excellent agreement with experimental data.

In the supercritical case (Fig. 11), the computed drag is the sum of boundary-layer momentum drag and wave drag. Again, there is excellent agreement with experimental data.

Figure 12 shows the effect of the different shock operators in the viscous case. In case of common nonconservative form, the wave drag was computed by pressure integration; this method fails absolutely with respect to drag prediction. The best result is obtained using the shock operator for oblique shock, as described here.

In Fig. 13, a calculated drag polar is compared with experimental data and calculated data of other authors. At the point $CL=0.8$, $M_\infty=0.73$, our calculated results agree very well with experimental results. For the other two points, our calculation with $M_\infty=0.73$ must give higher drag values than those of the experiment, as the experiment was conducted at lower Mach number $M_\infty=0.725$.

Computational Accuracy

The computation is done on the above-mentioned H-type grid with 101 points in the streamwise direction, 61 of which are on one side of the airfoil contour. The computational domain is 5 chords in each direction around the airfoil, i.e., approximately 11 chords in the x and 10 in the z direction. The first iterations are done on a crude grid with doubled mesh size. In the far field, the velocity potential is prescribed by the Prandtl-Glauert panel solution used for grid generation and the circulation is corrected by the transonic solution. Some tests were done with outer boundaries at a distance of 8, 12, and 20 chords. The results changed only within the overall computational accuracy for eight chords distance.

Some special tests were done on the accuracy of wave drag computation. The left part of Fig. 14 demonstrates that wave drag is nearly independent of grid spacing; the left point belongs to the normal grid with 61 points per chord, the right one to 29 points. The right part shows the convergence history for a solution cycle on crude and fine grid.

The difference equations were solved by a simple SLOR method. It takes 163 s of CPU time on an IBM 3081 for an inviscid problem with normal *PrOP*. For a viscous solution with oblique *PrOp*, the CPU time depends on problem (lift, transition, separation), but remains below 300 s on the same machine.

Extensions to Three Dimensions

A three-dimensional shock point operator and a three-dimensional shock/boundary-layer interference model are constructable by transforming the two-dimensional models to a direction normal to the shock. All we need is the sweepback angle of the shock. But the restriction to flows without shock-induced separation still remains. It is not yet known whether the limiting condition for shock separation is the normal preshock Mach number of about 1.3 as for two dimensions. Last but not least, for complete drag prediction, a three-dimensional inverse boundary-layer method must be available.

Conclusion

A method to predict transonic wave drag was presented, emphasizing the essential physical effects and simple coding.

It was shown that it is possible to describe the effects of entropy increase at the shock/boundary-layer interference within the framework of the full potential equation. This equation is strictly valid in the outer flowfield in front of the shock; it describes quite well the flow behind a weak shock when a so-called "Prandtl operator" is introduced at the shock location. This operator satisfies the Prandtl equation, which is the consistent jump condition at the shock. The remaining part of the Rankine-Hugoniot conditions gives the entropy jump to correct the pressure behind the shock.

The boundary condition of an inviscid shock is that it be normal at the wall. It must be replaced by the viscous boundary condition of the shock, which was shown to be a shock with a maximum deflection angle at the nonseparated boundary layer.

A full potential code with the improvements described above allows flow computation around airfoils with very accurate drag prediction. The code is fast and easy to handle. It is a powerful design tool, especially for modern transport aircraft.

Acknowledgment

This work was supported by the German Ministry of Research and Technology (BMFT).

References

[1] Bauer, F., Garabedian, P., Korn, D., and Jameson, A., "Supercritical Wing Sections, II," *Lecture Notes in Economics and Mathematical Sciences,* No. 108, Springer-Verlag, Berlin, 1975.

[2] Murman, E. M. and Cole, J. D., "Calculation of Plane Steady Transonic Flow," AIAA Paper 70-188, Jan. 1970.

[3] Murman, E. M., "Analysis of Embedded Shock Waves Calculated by Relaxation Methods," *AIAA Journal*, Vol. 12, May 1974, pp. 62-33.

[4] Rizzi, A. and Viviand, H., "Collective Comparison of the Solutions to the Workshop Problems," *Notes on Numerical Fluid Mechanics*, No. 3, Vieweg, Braunschweig, FRG, 1981, pp. 167-221.

[5] Chaderjian, N. M. and Steger, J. L., "The Numerical Simulation of Steady Transonic Rotational Flow Using a Dual Potential Formulation," AIAA Paper 85-0368, Jan. 1985.

[6] Chen, L. T., Vassberg, J. C., and Peavey, C. C., "A Transonic Wing-Body Flowfield Calculation with Improved Grid Topology and Shock-Point Operators," AIAA Paper 84-2157, Aug. 1984.

[7] Enquist, B. and Osher, S., "Stable and Entropy Satisfying Approximations for Transonic Flow Calculations," *Mathematics of Computation*, Vol. 34, 1980, pp. 45-75.

[8] Hafez, M., Habashi, W. G., and Kotinga, P. L., "Conservative Calculations of Non-Isentropic Transonic Flows," AIAA Paper 84-1182, June 1984.

[9] Hafez, M. and Lovell, D., "Entropy and Vorticity Corrections for Transonic Flow," AIAA Paper 83-1928, 1983.

[10] Klopfer, G. H. and Nixon, D., "Nonisentropic Potential Formulation for Transonic Flows," *AIAA Journal*, Vol. 22, June 1984, pp. 770-776.

[11] Lock, R. C., "A Modification to the Method of Garabedian and Korn," *Notes on Numerical Fluid Mechanics,* No. 3, edited by A. Rizzi and H. Viviand, Vieweg, Braunschweig, FRG, 1981, pp. 116-124.

[12] Lucchi, C. W., "Shock Correction and Trailing Edge Pressure Jump in Two-Dimensional Transonic Potential Flows at Subsonic Uniform Mach Numbers," AIAA Paper 83-1884, 1983.

[13] Melnik, R. E. and Brook, J. W., "The Computation of Viscid/Inviscid Interaction on Airfoils with Separated Flow," *Third Symposium on Numerical and Physical Aspects of Aerodynamic Flows,* edited by T. Cebeci, California State University, Long Beach, Jan. 1985, pp. 1-21-1-37.

[14] Osher, S., Hafez, M., and Whitlow, W. Jr., "Entropy Condition Satisfying Approximations for the Full Potential Equation of Transonic Flow," *Mathematics of Computation*, Vol. 44, No. 169, Jan. 1985, pp. 1-29.

[15] Klevenhusen, K. D., "Beitrag zur potentialtheoretischen Berechnung nicht isentroper Verdichtungsstöße im ebenen Fall," *Numerische Aerodynamik-Stand der Entwicklung in Deutschland*, DGLR-Bericht 84-01, 1984, pp. 121-126.

[16] Oswatitsch, K., *Grundlagen der Gasdynamik*, Springer-Verlag, Wien, 1976, Chap. V.12.

[17] Klevenhusen, K. D., "2-D Elliptic Grid Generation Using a Singularity Method and its Application to Transonic Interference Flows," *Numerical Grid Generation*, edited by J. F. Thompson, North Holland, Amsterdam, 1982, pp. 739-760.

[18] Huynh, H. and Jou, W. H., "Singularity Embedding Method in Potential Flow Calculations," AIAA Paper 82-0991, June 1982.

[19] Kwak, D., "An Implicit Transonic Full Potential Code for Cascade Flow on H-Grid Topology," AIAA Paper 83-0506, Jan. 1983.

[20] Courant, R. and Friedrichs, K. O., *Supersonic Flow and Shock Waves*, Interscience Publishers, New York, 1948.

[21] Bohning, R., *Die Wechselwirkung eines senkrechten Verdichtungsstößes mit einer turbulenten Grenzschicht an einer gekrümmten Wand*, Habilitation, Universität (TH) Karlsruhe, Karlsruhe, FRG, 1982.

[22] Bohning, R., private correspondence, 1984.

[23] Mertens, J., "Verhalten eines transsonischen Verdichtungsstoßes in Grenzschichtnähe," MBB-UT, Bremen, FRG, Rept. MBB/LFK 85010 5/FKS, March 1985.

[24] Delery, J. M., "Shock Wave/Turbulent Boundary Layer Interaction and its Control," *Progress in Aerospace Sciences*, Vol. 22, No. 4, Pergamon Press, Oxford, England, 1985, pp. 209-280.

[25] Dargel, G., "Berechnungsverfahren für viskose transsonische Profilströmungen SGW," MBB-UT, Bremen, FRG, Rept. MBB/LFK 8213 6/NEW II, Sept. 1985.

[26] Thiede, P., Dargel, G. and Elsholz, E., "Viscid-Inviscid Interaction Analysis on Airfoils with an Inverse Boundary Layer Approach," *Recent Contributions to Fluid Mechanics*, edited by W. Haase, Springer-Verlag, Berlin, 1982, pp. 244-252.

[27] Alber, I. E., "Similar Solutions for a Family of Separated Turbulent Boundary Layers," AIAA Paper 71-203, 1971.

[28] Walz, A., *Boundary Layers of Flow and Temperature*, Massachusetts Institute of Technology Press, Cambridge, 1969.

[29] Otte, F. and Thiede, P., *Berechnung ebener und rotationssymmetrischer kompressibler Grenzschichten auf der Basis von Integralbedingungen*, Fortschritt—Berichte der VDI Zeitschriften, Reihe 7, Nr. 33, 1973.

[30] Thiede, P., *Kriterien zur Vorausbestimmung des laminarturbulenten Grenzschichtumschlages an umströmten Körperkonturen*, Forschritt—Berichte der VDI Zeitschriften, Reihe 7, Nr. 31, 1972.

[31] Harris, C. D., "Two-Dimensional Aerodynamic Characteristics of the NACA 0012 Airfoil in the Langley 8 Foot Transonic Pressure Tunnel," NASA TM 81-927, April 1981.

[32] Firmin, M.C.F., Cook, P. H. and McDonald, M. A., "Airfoil RAE 2822 Pressure Distribution and Boundary Layer Measurements," AGARD-AR-138, 1979.